Sculpting crystals one Burgers vector at a time: Toward colloidal lattice robot swarms

Bryan VanSaders[a] and Sharon C. Glotzer[a,b,c,1]

[a]Department of Materials Science and Engineering, University of Michigan, Ann Arbor, MI 48109; [b]Department of Chemical Engineering, University of Michigan, Ann Arbor, MI 48109; and [c]Biointerfaces Institute, University of Michigan, Ann Arbor, MI 48109

Contributed by Sharon C. Glotzer, November 30, 2020 (sent for review August 17, 2020; reviewed by John C. Crocker, David G. Grier, and Jim Pfaendtner)

Plastic deformation of crystalline materials with isotropic particle attractions proceeds by the creation and migration of dislocations under the influence of external forces. If dislocations are produced and migrated under the action of local forces, then material shape change can occur without the application of surface forces. We investigate how particles with variable diameters can be embedded in colloidal monolayers to produce dislocations on demand. We find in simulation that when embedded clusters of variable diameter particles are taken through multiple cycles of swelling and shrinking, large cumulative plastic slip is produced by the creation and biased motion of dislocation pairs in the solid for embedded clusters of particular geometries. In this way, dislocations emitted by these clusters (biased "dislocation emitters") can be used to reshape colloidal matter. Our results are also applicable to larger-scale swarms of robotic particles that organize into dense ordered two-dimensional (2D) arrangements. We conclude with a discussion of how dislocations fulfill for colloids the role sought by "metamodules" in lattice robotics research and show how successive applications of shear as a unit operation can produce shape change through slicing and swirling.

active matter | swarming | colloids | robotics | soft matter

With sufficient miniaturization it is possible to create materials that at the human length scale appear continuous but are in fact composed of discrete subunits that have been engineered. When the subunits are small and relatively simple, such materials are often referred to as "metamaterials." As an example, the manipulation of optical material properties by engineering the response of so-called "metaatoms" has seen significant success (1, 2).

When the complexity of the subunit is increased to the point where each "module" has some combination of independent sensing, actuation, self-propulsion, and communication ability, then the material is described as a modular robot (3). Many forms of reconfigurable modular robots have been proposed and prototyped. A subset of studies frames the aggregate collection of robotic modules as a new metamaterial type. Lattice robots (4–6), "programmable matter" (7), the "slimebot" (8), and the "particle robot" (9) are examples of this school of thought. While simulations of modular robots have advanced to the million-module scale (10–12), experimental realization of more than 100 robotic modules in the laboratory remains challenging [with the notable exception of Rubenstein et al. (13)]. The demanding requirements of robotic function necessitate considerable complexity and cost, restricting experimental studies to the macroscopic scale.

Metamaterials and active matter, while conceptually linked, differ greatly in their subunit cost and in functionalities such as environment sensing, communication, or information processing capacity. In the last several decades, chemists have advanced techniques that permit submicrometer particles to perform work locally, increasing the functions available to very small subunits. For the first time, it is feasible to consider a continuum-scale material composed of devices (active particles) that locally perform work in a designed way. Swarms of self-propelled colloids can be controlled with a global field, such as light intensity (14), chemical signaling (15), or a rotating magnetic field (16–20). The behavior of such nonequilibrium colloidal swarms relies heavily on emergent phenomena to take the place of integrated communication and control often present in macroscale robotic swarms. Despite the stochasticity inherent in emergent interactions, certain actions are predictable, controllable, and repeatable.

A fundamental function of a modular robot is to reconfigure its shape. Many applications of interest rely on shape change: moving cargo, crawling past obstacles, engulfing cargo, etc. When the number of subunits is small and subunit complexity is high, algorithmic planning can achieve near optimal reconfiguration characteristics. For colloidal-scale metamaterials composed of many thousands or millions of individual subunits, with no ability to locally communicate or algorithmically plan their actions, another approach is needed. Shape change on this scale might be better thought of as a controlled plastic deformation. In systems composed of isotropically attracting subunits (such as colloidal crystals of sticky hard spheres or atomic metals), plastic deformation is controlled by the production and migration of defects known as dislocations (21, 22). The creation and control of two-dimensional (2D) dislocations via optical fields have been reported in colloidal systems (23, 24).

In this paper we explore how quasi-2D crystallites of colloids can be reshaped by the production and migration of dislocation defects. We present here a simplistic scheme of dislocation creation based on swelling the size of an anisotropically shaped subset of the crystallite's particles. This approach to material reconfiguration relies upon consistent creation of dislocations (in our study, at the surface of the embedded swellable

Significance

Colloidal nanoparticles that exert local forces suggest a future class of swarm metamaterials. These swarms must coordinate their actions to accomplish useful tasks, such as changing the shape of the swarm or engulfing an object. We use computer simulation to show how the coordination of active colloidal nanoparticle swarms can be simplified by harnessing crystalline defects. We demonstrate that with only a single degree of freedom (the diameter of a small fraction of particles) repeatable shape changes can be achieved in a 2D collection of particles with crystalline ordering and isotropic attraction. This work also relates to macroscopic robotic swarms, illuminating a mechanism for emergent control.

Author contributions: B.V.S. and S.C.G. designed research; B.V.S. performed simulations; B.V.S. analyzed data; and B.V.S. and S.C.G. wrote the paper.

Reviewers: J.C.C., University of Pennsylvania; D.G.G., New York University; and J.P., University of Washington.

The authors declare no competing interest.

[1]To whom correspondence may be addressed. Email: sglotzer@umich.edu.

This article contains supporting information online at https://www.pnas.org/lookup/suppl/doi:10.1073/pnas.2017377118/-/DCSupplemental.

Published January 11, 2021.

cluster) and a sink to absorb dislocations. The simplest such sink is a free surface of the material domain; however, other sinks include internal grain boundaries within extended crystalline domains or even other (complementary) dislocations. In this study we focus on the case of a finite-size crystallite domain as the material to be reconfigured and therefore use the material edges as the primary dislocation sink. Such finite-sized crystallites necessitate attractive interactions between the subunits. In a colloidal setting, such attraction might be supplied by depletion (25), electric fields (26, 27), magnetic fields (28), particle activity (14), DNA functionalization (29), or a variety of other tactics (30, 31). The important characteristic of the interparticle attraction here is isotropy. Strongly directional interactions will not permit the free motion of dislocations.

We simulate a colloidal crystalline monolayer of finite size, such as might be prepared by sedimentation of sticky colloidal spheres on a flat surface. A cluster of colloids with variable diameter [achieved via, e.g., heating (32, 33), solvent swelling (34, 35), or other methods (36)] is embedded in this monolayer. We show that global control over a single degree of freedom (the diameter of the particles in the embedded cluster) is sufficient to effect significant reshaping of the crystallite's boundary by the creation and emission of dislocations. Our results are also applicable to certain classes of "lattice robots," which operate at larger length scales (4, 5).

We begin with an overview of our concept to use dislocations to create colloidal shape shifters. Next, we show several examples of reshaping in finite-sized crystallites and bulk domains. We then present the necessary geometric features of the embedded clusters and the importance of anisotropy in dislocation emission. We conclude with a discussion of how this study relates to existing work on reconfiguration schemes for modular robots.

Dislocations as Colloidal Crystallite Reshaping Tools

We propose that by selectively inducing shear along arbitrary slip planes in a crystallite a wide range of surface and interior reconfigurations are possible. Fig. 1 outlines three cases where the ability to shear along arbitrary planes allows for a useful task to be carried out. Fig 1 shows how bulk locomotion, cargo transport, and cargo capture could be achieved using only shear displacements in a colloidal crystallite robot.

Within a crystalline material, nonelastic shear displacement is the result of the propagation of dislocations. Dislocations are the fundamental unit of shear slip in crystals undergoing plastic (i.e., irreversible) deformation. As a dislocation travels through a material, the regions on either side of the defect's glide plane are translated (slipped) relative to each other by an amount given by the dislocation's Burgers vector. The creation of a dislocation must conserve the total Burgers vector (which must remain zero if starting from a defect-free crystal). Therefore, when dislocations are created, they appear in pairs. For a given glide plane in a 2D crystal, such dislocations can be either left or right handed, which we refer to as "positive" and "negative." Positive dislocations are those that define the termination of an additional half plane of particles that extends into the positive half space of the crystal ("above" the glide plane). Likewise, negative dislocations terminate the half plane that occupies the negative half space ("below" the glide plane). The Burgers vector of these two dislocations is opposite and equal, and if they are brought together, they annihilate and a defect-free crystal results.

If a dislocation is migrated to a boundary of a crystal, such as exists at a free surface, then the termination of the half plane it bounds will appear on that surface. This eliminates the dislocation and its elastic deformation, leaving behind only the change to the surface. This change is a step of height equal to the dislocation's Burgers vector. If dislocation pairs could be created and driven to the surface in a particular (arbitrary) pattern, then in theory any surface reorganization could be accomplished one Burgers vector at a time. This method of surface reshaping requires the ability to produce oriented dislocations on demand as well as a means to direct them toward the free surface to be reshaped. Notably, if both the positive and negative dislocations from the created pair were directed to the same surface, then no permanent change in the crystallite boundary would be achieved because the second dislocation to arrive would reverse the effects of the first one. Therefore, to use dislocations as operations to sculpt surfaces we must have a means of separating them that is strong enough to overcome the attractive force driving recombination of the pair on the same glide plane.

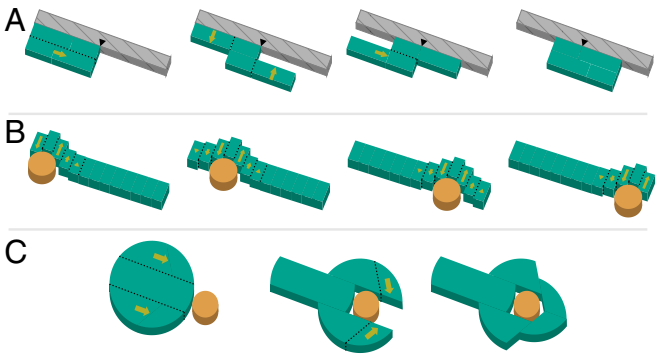

Fig. 1. Schematic representations of functional operations that can be performed by selective shearing. A crystalline colloidal robot (green) reconfigures itself by shearing along selective planes (dashed lines). Yellow arrows represent planned displacements. (*A*) Locomotion via shearing for a colloidal robot in contact with a wall (gray, hatched). By shearing on multiple planes the robot is "rolled" along the wall. (*B*) Peristaltic transport of an object (yellow cylinder) by a colloidal robot via shearing operations. By sequential activation and reversal of shearing planes, the cargo is transported along the robot. (*C*) Cargo (brown cylinder) capture via shearing operations.

The fundamental unit of dislocation-based reconfiguration is a cycle in which the dislocation pair is produced by a dislocation emitter and subsequently absorbed by dislocation sinks. We demonstrate this process schematically in Fig. 2. Fig. 2 *B*, *i–iii* shows schematic representations of dislocations in a monolayer near the edge of an embedded variable-diameter cluster (dislocation emitter). As the diameter of the particles in the emitting cluster is increased, a dislocation pair is created at one of the cluster corners. This process can be rationalized as the extension of the cluster side forcing a misregistry of crystal lattice planes across the line defined by the edge of the cluster. This misregistry manifests as a pair of complementary dislocations. While the size of the embedded cluster is large, stress-mediated forces drive the negative dislocation away from the cluster, toward the material edge where the dislocation is absorbed. The complementary, positive dislocation remains trapped on the emitter cluster edge. Later in the operating cycle, the embedded cluster shrinks, which drives the positive dislocation away. If the positive and negative dislocations are absorbed by different free surfaces, then a finite quantity of slip (one Burgers vector) is introduced along the crystal plane defined by the edge of the emitter cluster. To see a video of this process with a hexagonal emitter cluster, see Movie S1.

To enact cumulative change by the motion of dislocations, their creation and migration must be repeatable and consistent. Dislocations must only be produced along desired edges of the cluster. Furthermore, the positive and negative dislocations must be repeatably separated. The cluster geometry shown in Fig. 2 lacks geometrical asymmetry which would ensure consistent operation as a dislocation emitter. Several forms of anisotropy are needed to produce dislocations on one plane only

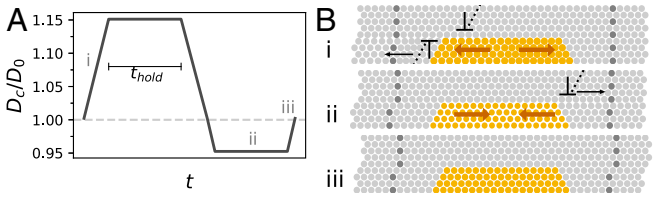

Fig. 2. (*A*) The diameter of variable-diameter particles over the course of a dislocation production cycle. (*B*) Cartoon representations of dislocation creation and migration at the edge of a cluster of variable-diameter particles (yellow). (*B*, *i*) A point in time just after a dislocation pair has been created at one corner of the embedded cluster. The expansion of the sides of the cluster has forced a misregistry of lattice planes above and below the plane defined by the edge of the cluster. This misregistry results in the creation of two complementary dislocations. The expanded size of the cluster drives the lower dislocation toward the free edge of the material. (*B*, *ii*) A point during the shrinking phase of diameter change. Shrinking drives the remaining dislocation toward the edge of the material. (*B*, *iii*) The final result of a successful cycle. Tracer particles (dark) show that a finite amount of slip has been produced on the plane defined by the edge of the embedded cluster.

and to repeatably bias their emission. The majority of this study is concerned with the geometrical features required to consistently produce shear deformation at the edge of an embedded cluster. In later sections we discuss the process by which cluster shape can be designed to yield optimal performance as a dislocation emitter. However, we begin by demonstrating some of the reconfigurations possible through dislocation control, deferring discussion of the design of cluster shape.

Results

Reconfiguration by Embedded Clusters Designed for Shear on a Single Plane. We demonstrate the action of optimized dislocation emitting embedded clusters through molecular dynamics (MD) simulation of particle monolayers. Unless otherwise noted, these monolayers are finite sized, and free edges are used as dislocation sinks. The crystallites are confined to a plane by a downward force and a repulsive force from a plane supporting it. This configuration mimics a sedimented colloidal layer (but neglects any effect of surface friction). Embedded clusters compose a small subset of particles (colored yellow) within the crystallite held together via harmonic bonds. Bonding eliminates the possibility of cluster reconfigurations occurring upon successive swelling cycles. It also results in a cluster that behaves as a connected body, which may be appropriate for experimental realizations in which a cluster is prefabricated as a single object and then embedded into a colloidal monolayer.

We first demonstrate the action of an embedded cluster geometry which was optimized to produce shear slip along a single glide plane. This optimal geometry involves two subclusters, with slightly different shapes (explained in detail in later sections). Fig. 3*A* shows the state of a crystallite ($N = 23,231$) with one pair of embedded subclusters after many swell/shrink cycles (Movie S2). As subsequent pairs of dislocations are produced and migrated to the edge of the crystallite, the domain is sheared in half. This shearing also produces a net torque on the crystallite, which rotates it. The handedness of this torque is opposite to that of the torque that would result if this crystallite was sheared by the application of surface forces.

A key consideration in the shearing operation is the distance of maximum separation of the dislocation pair. If this distance is smaller than the dimensions of the crystallite, then the dislocations may not reach the boundary. Dislocations that do not reach the boundary remain in the system and may interfere with subsequent cycles. This can happen either through backward migration (particularly the negative dislocation, which can be reattracted to the cluster from long range) or by producing a "back pressure" that resists additional dislocation pair creation. We find that backward migration is a larger problem than back pressure, because in a back-pressure situation subsequent cycles tend to create short-lived dislocation pairs that push the original pair farther away, eventually clearing defects from the vicinity of the cluster over several cycles.

A related failure mode that we observed is for several vacancies to condense around the embedded cluster, rendering subsequent cycles ineffective in generating dislocation pairs. If the minimum particle diameter of the shrinking phase is too small, then cross-slip events occur whereby the negative dislocation decomposes into vacancies that attach to the surface of the cluster. Such attached vacancies "poison" the cluster, preventing subsequent defect production. We were able to suppress this process by increasing the minimum size of the variable-diameter particles, so that additional defects were not produced during the shrinking phase (see Fig. 5*A* for discussion of the thresholds of defect creation during the swelling and shrinking phases). However, below this size we observed farther migration of the negative dislocation during t_{hold} (Fig. 2). We found that the forces driving dislocation migration away from the cluster also are a function of the cluster geometry, particularly the double-subcluster arrangement (discussed below).

Shearing on Multiple Planes Simultaneously. Multiple shearing clusters can be combined together to carry out more complex deformation operations in crystallites. Here we show two such kinds of compound operations. In this study, we did not introduce any phase delay between the swelling cycles of the

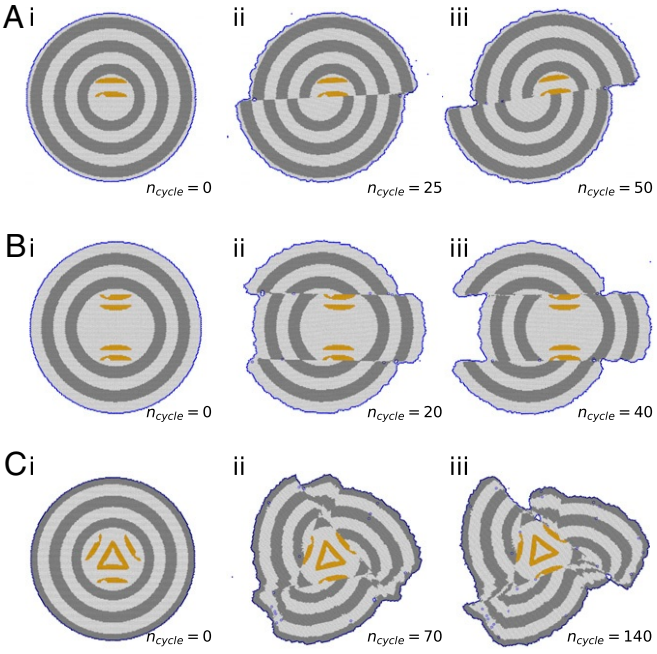

Fig. 3. Cyclic operation of dislocation-producing clusters (yellow) embedded in circular crystallites. Dark rings are guides to the eye for tracking plastic deformation, and blue particles have fewer than six nearest neighbors. (*A*) A single embedded cluster pair, causing shear across one plane. Snapshots at 0 (*i*), 25 (*ii*), and 50 (*iii*) cycles are shown. (*B*) Two embedded cluster pairs in a polar configuration. Snapshots at 0 (*i*), 20 (*ii*), and 40 (*iii*) cycles are shown. (*C*) Three embedded cluster pairs in a chiral configuration. Snapshots at 0 (*i*), 70 (*ii*), and 140 (*iii*) cycles are shown. Cluster pairs operate together as a dislocation-producing unit. Cluster anisotropy, shape, and surface notching are critical design parameters for consistent dislocation production and are discussed below.

embedded clusters. Such a delay could be exploited to improve the efficiency and stability of multiple-cluster schemes. However, here we show that complex material reshaping is possible even without phase delay. For videos of these examples see Movies S3–S5.

Slicing. When two embedded shearing clusters are arranged so that their glide planes are parallel and opposite in sign, then the slab of material contained between those glide planes is slipped relative to the rest of the crystallite. We refer to this kind of polar multiplane shearing as "slicing." Fig. 3*B* shows a nonchiral (note notch positions) slicing operation in a crystallite ($N = 23,321$) containing two pairs of embedded clusters. The even slip produced by the top and bottom clusters indicates that they are operating in tandem, without cross-interference. If the two clusters are placed closer to each other, then cross-slip events can occur with multiple dislocations recombining. This configuration can be thought of as transporting wave after wave of extra planes to the crystallite edge, which grows a protrusion on one side while excavating a cavity on the other. Unlike in the shearing example Fig. 3*A*, there is minimal net rotation of the crystallite here, because the forces produced by shear are balanced.

Swirling. When the emission directions of multiple embedded clusters in the same crystallite are arranged in a chiral manner (Fig. 3*C*, note the location of cluster notch), then a complex rotation of material in the crystallite can be accomplished. We term this chiral multiplane shearing operation as "swirling." The effect is to mix and translate sections of the crystallite past each other, resulting in a flower-like shape. Note that there is a net rotation of the crystallite, again in the opposite direction to that which would occur if this process were accomplished with surface forces. The efficiency (plastic slip per swell–shrink cycle) of this operation is significantly lower ($\approx 1/3$) than that of the other operations we have discussed. This is due to the tendency of clusters to suppress the splitting of other clusters' dislocation pairs, resulting in many cycles where only one side of the triangular arrangement of cluster pairs succeeded in migrating its dislocation pair to the crystallite boundary. This kind of interaction may be suppressed by introducing a phase offset between the cycles of the three sides of the triangle. Despite this tendency for cross-interference between clusters, this example demonstrates that the biased pair production of the clusters is robust enough to produce the desired effect with a minimum of control.

Dislocation Emission in a Periodic Domain. In a small crystallite, the crystal surface acts as a sink for both positive and negative dislocations, capturing them and thereby permitting future cycles to release new dislocation pairs into undistorted crystal regions. However, dislocations can be absorbed by other crystal defects as well.

Fig. 4 shows a slicing configuration of clusters embedded in a periodic crystalline domain ($N = 40,000$). The size of the periodic domain was chosen so that for a perfect crystal (at the temperature of simulation) the pressure is zero. As dislocations are produced, they traverse the periodic boundaries of the box and recombine on the opposite side of the cluster they were created on. This can also be thought of as clusters passing dislocations to their periodic images in adjacent periodic domains. The example shows that multiple clusters on the same glide plane act as "repeaters," absorbing their neighbors' dislocations. In a real crystal, a line of repeaters therefore should be able to transport dislocations over very long ranges. Because the line of repeaters here is made of periodic images, there is no phase delay between the cycles of adjacent clusters. Much like the chiral demonstration above, we expect that introducing a phase delay could improve the operational robustness of a line of repeaters.

Designing High-Performance Embedded Cluster Geometries. We now take a closer look at the geometry of embedded clusters

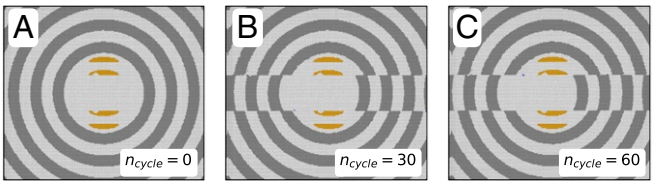

Fig. 4. Cyclic operation of two pairs of clusters (yellow) embedded in a periodic domain. Clusters "pass" dislocations to their images, resulting in a slip band. (*A*) The initial configuration, before any swell/shrink cycles. Dark rings are guides to the eye for tracking plastic deformations, and blue particles have fewer than six nearest neighbors. (*B*) System configuration after 30 cycles. (*C*) System configuration after 60 cycles.

well suited to inducing shear displacement over many cycles. Good cluster performance depends on several metrics. First, the dislocations must be produced only on one glide plane. Once produced, the dislocation pair must be separated as far as possible, so that the dislocations can reach a surface or other recombination site. Finally, the dislocation pair must be created and separated with the same polarity; i.e., the positive and negative dislocations should leave in the same direction on each cycle. We now examine the connection between cluster geometry and performance through each of these three metrics.

Extensional threshold of defect creation. As embedded clusters swell, the extension of their edges induces crystal plane misregistry, which eventually nucleates a dislocation pair. To understand the thresholds for dislocation creation we first study an embedded cluster with a high aspect ratio rectangular geometry. Expansion of the cluster sides due to isotropic swelling of the constituent particles produces shear stress that eventually results in the creation of a dislocation pair. Consider the effect of length extension, $\Delta l/D_0$. Fig. 5 shows defect number and strain field magnitude data for rectangular clusters subjected to isotropic particle swelling or shrinking. In these simulations defects are tracked by identifying particles that have Voronoi cells without six sides. For particles with six Voronoi neighbors a local affine strain can be calculated using the Voronoi polygon vertices (37). For snapshots of the Voronoi diagram, see *SI Appendix*.

Fig. 5*A* shows the number of defects ($N_{defects}$) observed for different states of cluster extension or contraction. Fig. 5 *A*, *Inset* shows a rendering of the rectangular cluster. A clear threshold in defect creation can be seen at an extension of $\Delta l/D_0 \approx 2$ and a contraction of $\Delta l/D_0 \approx -1.5$. For extension, only five (C_5) and seven (C_7) coordinated defects are created, which is consistent with the core of a dislocation. For contractions, other coordinations (C_4, C_8) are also found. The dislocation dipole that is emitted from a shrinking rectangle cluster represents a missing partial plane of particles. These types of dislocation dipoles (vacancy, or intrinsic, dipoles) are unstable in this system, and we observed that they often decomposed into immobile vacancy clusters, which is why more varieties of defect coordinations are observed for cluster contraction. In contrast, during cluster swelling the emitted dislocations represent the extra plane of particles that must be ejected to make space. Such interstitial (or extrinsic) type dislocation dipoles are more likely to leave the vicinity of the expanding cluster, leaving behind a bound pair of complementary negative dislocations on the embedded cluster surface.

Fig. 5*B* shows the value of the largest affine shear strain (η_{xy}) found around the rectangular cluster for various extensions and contractions. For extensions below the threshold, maximum shear strain scales in a superlinear fashion. At the threshold extension, maximum shear values dramatically increase. For

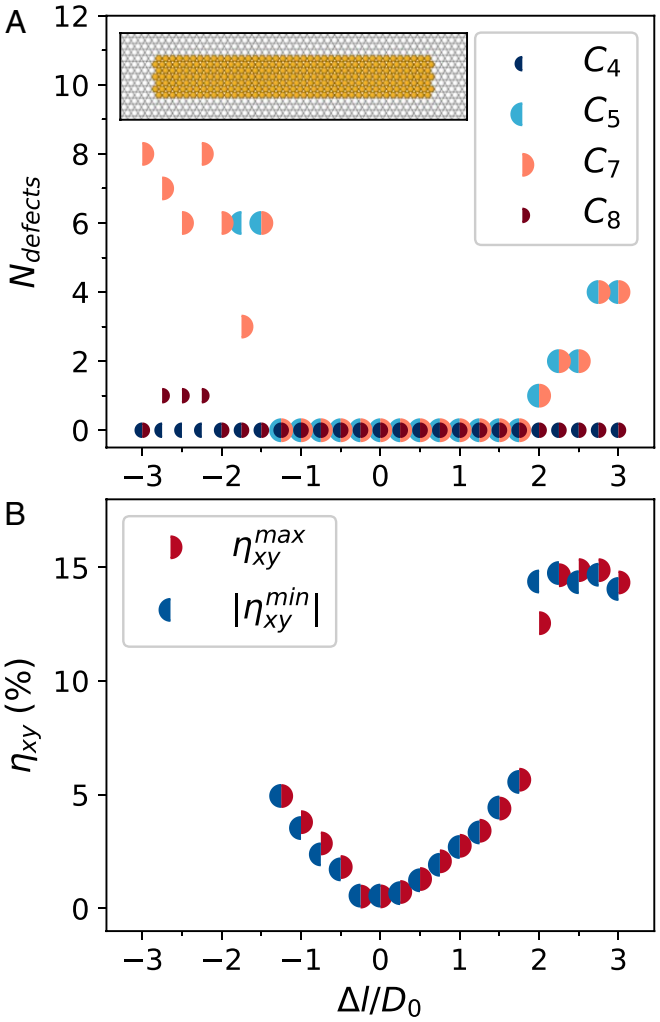

Fig. 5. Extension and shear thresholds for creation of defects. (*A*) The number of 4-, 5-, 7-, and 8-coordinated particles (C_4, C_5, C_7, and C_8), as found from the Voronoi diagram of the crystal. *Inset* shows a rendering of the rectangular embedded cluster. (*B*) Maximum affine shear strain magnitudes for a rectangular cluster. The creation of dislocation defects coincides with shear strains of $\approx \pm 5\%$.

extensions, this increase is to the value of affine strain calculated near the core of a dislocation. For contractions, very large strain magnitudes are found due to the presence of highly distorted vacancy cluster environments. The behavior of the strain magnitudes below the yielding point indicates the cause of the extension/contraction asymmetry. For the pair potential used here, tension and compression have different material stiffnesses resulting from the fundamental asymmetry of the pair potential bonding well. Such strain asymmetry can be manipulated through changing either the shape of the pair potential or the statepoint of the material (37).

Controlling dislocation emission. To avoid the creation of extraneous dislocations, we desire an embedded cluster geometry that produces a single dislocation pair on one glide plane with high repeatability. When the boundary of an embedded cluster is aligned with a slip plane in the crystal, dislocations tend to be created along that boundary provided that the extension due to particle swelling is sufficiently large. Therefore, to minimize the alignment of all but one cluster edge with slip planes, we employ a half-ellipse–shaped cluster. The single flat edge of the cluster is aligned with a slip plane which we denote as (00). Other planes exist within the same low-energy slip system; for symmetric half ellipses there are two other equivalent planes which we refer to as (01) and $(0\bar{1})$.

We quantify the propensity of shear strain on a slip plane to produce a dislocation, using the negative autoconvolution of the shear field sampled around a cluster at swelling values below the defect creation threshold. For a shear field with perfect inversion symmetry on a slip plane, the maximum of the negative autoconvolution will be

$$A_{max} = max(\eta_{xy}(x)^* - \eta_{xy}(x)) = \sum_x \eta_{xy}^2(x) \qquad [1]$$

which is proportional to the shear energy density integrated along that slip plane (in the linear elastic limit). We use A_{max} to identify which slip planes are likely to create dislocations as the shear strain threshold is approached. Fig. 6*A* shows A_{max} with respect to the position of the half-ellipse cluster. The two families of slip planes are shown. The (00) family contains the largest peak, at the flat bottom edge of the ellipse, with a secondary peak at the top of the rounded cluster. The rounding of the cluster suppresses dislocation emission from the top surface. Also shown is A_{max} for the (01) slip planes. This slip plane generally has a smaller propensity for dislocation emission than the designed (00) plane. However, as the ratio of length l to width w of the half-ellipse cluster is changed, the difference between

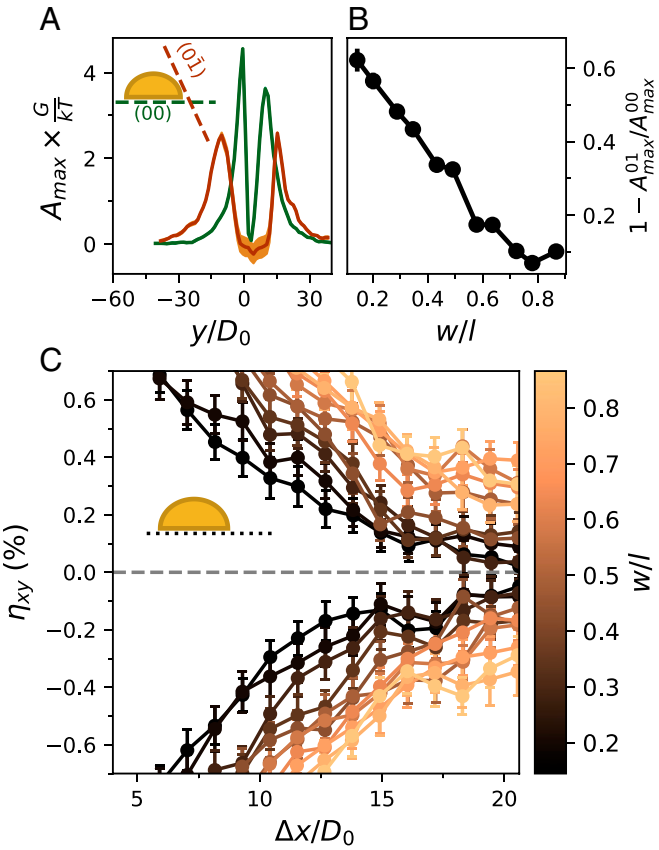

Fig. 6. Strain fields around single half-ellipse clusters. (*A*) Maxima of the negative shear autoconvolution, converted to energy units using the linear shear modulus (G). The values for (00) (green) and (01) (brown) family planes are shown. Uncertainty is represented with shaded bounding curves for both lines. (*B*) The relative difference of peak negative shear autoconvolution between slip families as the width of the half ellipse is increased. (*C*) Shear strain along the primary glide plane for single half-ellipse clusters of aspect ratios.

the primary (00) peak and the (01) peak decreases relative to the (00) maximum (Fig. 6*B*). This means that wide half ellipses are prone to spurious emission of dislocations into the (01) slip planes. To ensure that single dislocations are produced with high repeatability, narrow half-ellipse clusters with as small as possible w/l ratios should be used. For plots of shear strain and negative shear autoconvolution around embedded clusters, see *SI Appendix*.

Ensuring dislocation pair separation. After dislocations are created by the swelling of an embedded cluster, they are driven to leave the vicinity of the cluster by the strain fields present around it. During swelling (shrinking), the positive (negative) dislocation is driven away from the embedded cluster. If the pair of dislocations are allowed to recombine, then no net slip will result. Therefore, it is important that the dislocation pair be as widely separated as possible. The forces that primarily motivate the motion of dislocations come from shear strain interactions. We sample the magnitude of shear strain present on the primary ((00)) glide plane near a single half-ellipse cluster (Fig. 6*C*). For embedded clusters of a given length and different aspect ratios, as width is increased the shear strain along the primary slip plane reaches farther. Therefore, wider (and thus larger) clusters are better at forcing dislocations to glide away.

Double half-ellipse clusters. By examining the trends of embedded clusters with a half-ellipse shape we have concluded that clusters with larger areas (i.e., lower aspect ratios) are more effective at sweeping dislocations from their vicinity. However, low aspect-ratio clusters are more likely to produce extraneous dislocations on other slip planes. To balance the advantages of large and small half-ellipse clusters, we propose a double half-ellipse cluster shape. In this geometry two half ellipses, separated by a vertical offset, function as a single dislocation-producing unit. This geometry has several advantages over the single half-ellipse cluster.

First, double half-ellipse clusters have a reduced tendency to emit extraneous dislocations compared to single half ellipses of the same total area. Fig. 7*A* shows the negative shear autoconvolution maxima for the (00) and (01) family of slip planes. Fig. 7*B* shows the relative difference between the maxima for the (00) family and the (01) family as a function of the vertical separation between the half ellipses. The red horizontal line indicates the relative difference for a single half ellipse of the same area. For small separations, the relative likelihood of extraneous emission is similar to that of a single half ellipse with the same total area. However, for larger separations, the relative difference between maxima in the (00) family and (01) family is increased above the case of a single half ellipse.

Second, the driving shear strain that pushes dislocations away from the embedded cluster is increased at long range for the double half-ellipse cluster geometry compared to the single ellipse. Fig. 7*C* shows the shear strain present on the primary slip plane as a function of distance to the cluster edge for double half ellipses. The red curve is the shear strain (from Fig. 6*C*) of a single half ellipse with the same total area. For large vertical separations ($\Delta y/D_0 > 20$) the shear strain at long ranges is similar to or less than that from a single half ellipse. However, for small and moderate separations ($\Delta y/D_0 < 20$) the shear strains, especially at long range, are larger in magnitude for the double half-ellipse geometry than the single half ellipse. This is a larger effect for positive strains, another result of the tension–compression asymmetry present due to the nature of the particle pair potential. The increased shear strain magnitude at long range is a result of the additional flat edge of the second half ellipse. This feature produces more shear strain than the relatively flat sides of a wide single half ellipse (see *SI Appendix* for plots of shear strain).

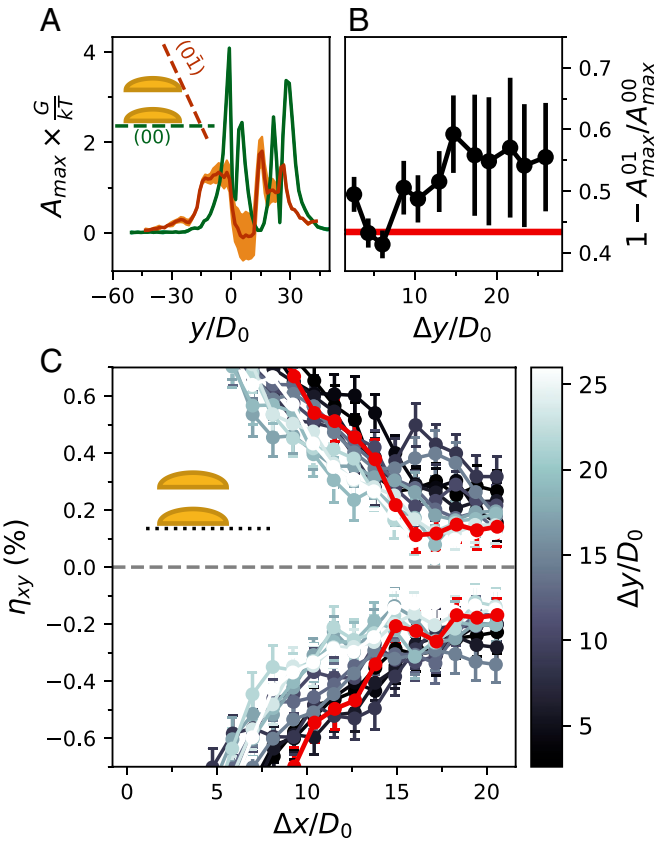

Fig. 7. Strain fields around double half-ellipse clusters. (*A*) Maxima of the negative shear autoconvolution, converted to energy units using the linear shear modulus (*G*). The values for (00) (green) and (01) (brown) family planes are shown. Uncertainty is represented with shaded bounding curves for both lines. (*B*) The relative difference of peak negative shear autoconvolution between slip families as the separation between the top and the bottom half ellipse is increased. The red line is the relative difference (from Fig. 6*B*) for a single half ellipse with the same area. (*C*) Shear strain along the primary glide plane for double half-ellipse clusters with different offsets. The red line is the shear strain (from Fig. 6*C*) for a single half ellipse with the same area.

Biasing dislocation emission. By investigating the thresholds for dislocation creation as well as the distribution of shear strain around the embedded cluster, we arrive at a cluster design that produces and drives dislocations reliably on one slip plane. To enact cumulative change to the crystallite's surface, dislocations of opposite handedness must be consistently emitted in opposite directions. One way to accomplish this biasing is to make a notch in the cluster edge that defines the primary slip plane. This breaks the reflection symmetry of the cluster and results in biased dislocation emission. Fig. 8 shows the slip accumulated in crystallites ($N = 13,051$) containing embedded single half-ellipse clusters. As the notch in their primary slip plane is shifted from the center of the cluster, dislocations are more likely to be emitted directionally depending on their handedness, resulting in cumulative slip.

The notch causes two related effects that are responsible for biased emission. First, when the notch is close to a corner, it reduces the likelihood of dislocation pair creation at that corner. For the primary slip plane, this means that the dislocation pair is first created at the corner farthest from the notch. The positive dislocation is then swept from the vicinity of the cluster by compressive strain fields.

Second, we find that the notch also tends to attract the negative dislocation during the shrinking phase of the cycle. This

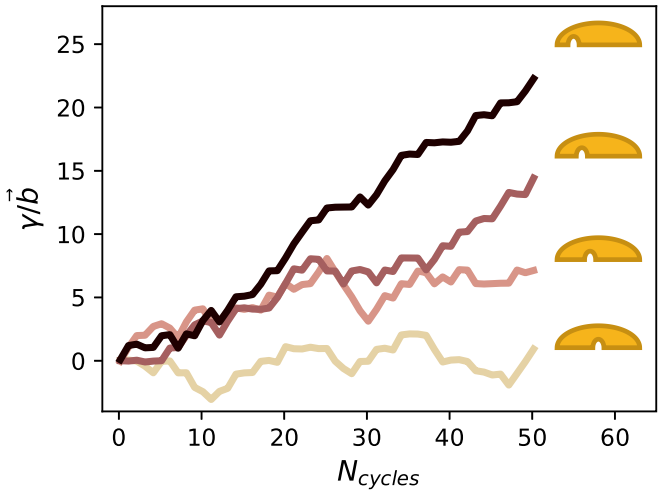

Fig. 8. Biasing of dislocation emission. Shown is cumulative slip over 50 cycles for clusters with different degrees of notch asymmetry. Greater asymmetry of the edge that defines the primary slip plane leads to greater robustness of dislocation pair splitting.

often results in the negative dislocation leaving the cluster from the notched side and thereby splitting the dislocation pair apart. The attraction of the negative dislocation to the notched side of the cluster as it returns from its maximum swelling diameter is a less consistent effect than that of the notch on the location of initial pair creation. As such, this attraction can limit the efficiency of dislocation pair splitting. This symmetry-breaking effect was found to be insensitive to the shape of the notch.

The Geometry and Action of High-Performing Clusters. High-performing dislocation-emitting clusters combine the features described above. For a detailed diagram of the highest-performing embedded cluster we found in this study, see *SI Appendix*, Fig. S4. We employ embedded clusters composed of double half ellipses with length $l = 30D_0$ and width $w = 6\sqrt{3}D_0/2$. The swelling and shrinking diameters ($\eta_p D_0$ and $\eta_n D_0$, respectively) of constituent particles were chosen to produce a length extension of $\Delta l_p = l(\eta_p - 1) = 2.0$ and $\Delta l_n = l(\eta_n - 1) = -1.2$. Fig. 9 shows several important steps in the swell/shrink cycle of the high-performance cluster geometry. In Fig. 9, the Voronoi cells around each particle are shown as polygons. Non–6-coordinated particles are colored by their Voronoi cell vertex number. Fig. 9*A* shows a time during cluster swelling immediately after dislocation pair creation. We see that the pair was created at the leading edge. Stresses at the trailing edge also produced particles with disturbed coordination shells, but this dislocation pair will quickly recombine. Fig 9*B* shows a time during the maximum diameter hold. During this time the negative dislocation remains trapped near the cluster, while the positive dislocation migrates away to escape the compressed environment near the cutting edge. Fig. 9*C* shows a time during the minimum diameter hold part of the cycle. During this hold, the negative dislocation is repelled by the tensile environment around the cluster. If the positive dislocation had not migrated far enough away from the cluster during the maximum diameter holding phase, then it could be attracted back during this part of the cycle. Due to the intrinsic tension–compression asymmetry of the shifted Lennard-Jones pair potential used for particle interactions, driving the negative dislocation to migrate is the limiting step. Driving the positive dislocation is comparatively easy. See Movie S6 for a video of this process.

Discussion

We have shown how controlled production of dislocations can be used to change the shape of a colloidal crystal monolayer. Beyond the results we have presented, several aspects of this method warrant discussion. We then explore the relationship between our method and those used in swarm robotics studies.

Reversibility of Operation. In this study, particles of tunable diameter are bonded together into clusters and so considered as permanent, although flexible, units. The direction of dislocation emission biasing is entirely set by the geometry of the cluster, in particular by the placement of the notch (*SI Appendix*, Fig. S4*C*). To have a cluster that can reverse its direction of biased dislocation emission, it would be necessary to have a cluster in which the notch can be changed in situ. This could be achieved by using a multiplexing scheme where there are three types of particles that can be independently swelled and deswelled. One type would comprise the majority of a cluster with two notches. The other two types would fill these notches. By activating the main body of the cluster and only one of the notches, the direction of operation of the cluster could be selected.

The Role of Temperature. Temperature plays an important role in the process of splitting a dislocation pair via elastic forces. The influence of temperature comes into play in several ways. First, as the embedded cluster changes size, it imposes long-range distortions to the crystal that drive the motion of dislocations. The magnitude of thermal fluctuations in the strain field sets the range at which the embedded cluster's strain field is effective at motivating dislocation motion. At low (high) temperatures, the influence of the cluster is strong (weak) relative to thermal fluctuations far from the cluster. However, at lower temperatures dislocations and vacancies are less mobile. Therefore, they

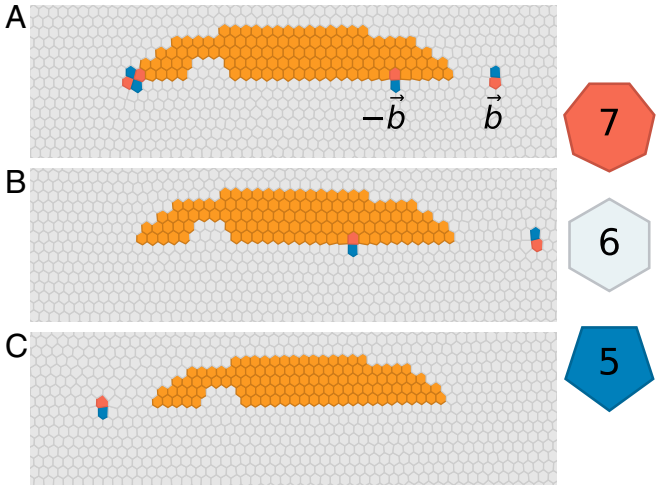

Fig. 9. Important points in the swell/shrink cycle of a notched half-ellipse cluster. Voronoi cells surrounding each particle are shown colored by their Voronoi coordination, *C* (or yellow, if representing a variable-diameter particle). (*A*) The initial split of the dislocation pair has just occurred during the swelling phase. Another dislocation pair can be seen at the left edge of the embedded cluster; however, this pair quickly recombines. (*B*) During the large diameter holding phase, the negative dislocation remains trapped on the cluster surface while the positive dislocation is repulsed by the compressed environment of the swollen cluster. (*C*) As the cluster shrinks to its original diameter and below, the negative dislocation is drawn toward the notch end and then repelled from the tensile strains present around the shrunken cluster.

will not be able to naturally diffuse and heal out, meaning that an escalating pileup of damage due to cluster cycling is more common. The temperature used in this study represents a compromise between the beneficial and adverse effects of low temperature. We expect that in addition to temperature, the depth and steepness of the interaction potential can be tuned to achieve similar effects. There likely exist particle interactions that produce much better dislocation mobility characteristics (i.e., a pair potential with a more symmetric attractive well).

Nonzero temperatures further enable the transport of material through the crystal via diffusive means, as well as by free-surface hopping. Such effects could become important for long timescales or temperature scales approaching the melting transition of the material. Under such conditions, the shape changes produced by the action of dislocation-emitting clusters would be working against diffusion-driven shape changes, which would favor high-symmetry (i.e., circular) crystallite shapes. The production and migration of dislocations can occur at zero temperature (when all diffusive motion is frozen out), driven entirely by the mechanical stresses applied via the swelling cluster. Therefore, the balance of thermally driven mass transport and dislocation-mediated mass transport can be tuned with some freedom. In the results presented here, we exploit a balance of temperature where surface diffusion of crystallites is minor on the timescales of simulations, but the temperature is still high enough to have some beneficial effect in "healing" undesirable defect pileups.

For the results presented here, each dislocation-producing cycle lasted approximately 10 times longer than the characteristic diffusion time of a Brownian particle (as determined by the ratio of particle diameter and self-diffusivity, $\tau = R^2/D_{self}$) (38). This timescale is the minimum cycle time that we found to be effective in reliably allowing dislocation pairs to separate and absorb to sinks. Fundamentally, the nature of the dislocation emission cycle would not be changed by increasing its duration manyfold. However, at sufficiently long timescales, competition from bulk diffusion of particles in the material could combat shape change. This range of time is far outside the scale investigated here.

Swellable Particles in Vitro. In theory, many polymer-based colloids could be swollen by changing their solvent environment. The surrounding bath's composition would be changed over the course of one cycle to create cyclic particle expansion. Therefore, the time required for each cycle would depend upon the maximum rate that the solvent's composition could be changed (without introducing bulk flows that destroy the colloidal crystallite). Highly swellable particles such as produced by coating a gold nanoparticle with DNA surface ligands (35) suggest the possibility to engineer particle response in terms of both solvent concentration and species. While chemical swelling may be rate limited by mass transport in the solvent, it lends itself readily to sensing applications in a biological or microfluidic environment. Additionally, a class of hydrogels based on poly(*N*-isopropylacrylamide) (poly(NIPAM)) opens the possibility for thermally or optically swellable particles (32, 33, 36). Nanoparticles that are both chemically and thermally responsive have also been demonstrated (34).

In the present study, particle size changes of 20% were found optimal for robust defect creation. Poly(NIPAM) particles are frequently reported to be capable of 100% or greater particle diameter changes near room temperature (32), far in excess of what is required for defect creation. Similarly, DNA-coated gold particles have been reported to be capable of 40% or more interparticle spacing change based on solvent environment (35). The required per-particle swellability for defect creation is set by the ratio of the embedded cluster's longest dimension and the lattice spacing of the crystal. Therefore, if a cluster is composed of many small particles, the per-particle diameter change required to produce defects will be even less than the 20% used here. An additional concern is changes to the stiffness of particles during swelling. In this study all particles are treated as effectively hard; however, in practice the compliance of particles changes with swelling (39). If particles in the swollen state have elastic properties comparable to those of the colloidal crystal, then they may be too compliant to impose the required strain which drives defect creation. However, this is unlikely, since the elastic properties of nearly all conventional solids are many orders of magnitude larger than colloidal materials due to the small size of atoms. Poly(NIPAM), for example, has a Young's modulus of several kilopascals even in its most expanded, compliant state (39) (see the following section for a discussion of colloidal crystal strength).

The embedded cluster of swellable particles that produces dislocations could be created through a variety of tactics. Individual arrangements of swellable particles can be prepared, for instance, using optical holography (40). However, the real potential of the proposed scheme would be realized by preparing the embedded clusters as a prefabrication step, perhaps by templated assembly (41). Once assembled they would be available as a bonded cluster for addition into a passive colloidal layer, during the growth of that layer. An alternative fabrication method would be to simply produce a monolithic object of the correct size and shape using lithographic methods, which may permit straightforward creation of arbitrary numbers of prefabricated dislocation emitters.

Material Strength of Colloidal Robots. The ultimate mechanical strength of a reconfigurable material is a result of both the bonding strength between subunits and the energetics of plastic deformation (42). The Young's modulus of the 2D material presented here can be estimated from the pair potential used to model attractive interactions. In 2D, under the harmonic solid approximation, the Young's modulus $Y = d^2U/dr^2(r = r_0)$, where U is the isotropic pair potential, and r_0 is the resting length of the interparticle bond. This measure has units of energy per area (or force per length) in 2D. For the pair potential used here the value of Young's modulus is $Y \approx 28 \times \epsilon/D^2$, where ϵ is a parameter of the Lennard-Jones potential describing the bonding energy well depth and D is particle diameter. For larger bonding energy values and smaller diameters, the stiffness of the material would increase. For 0.5-m colloidal particles at room temperature (with bonding strength $5\,k_bT$), this value is $\approx 10^{-6}\,\mathrm{N/m}$.

The ultimate strength of a material does not solely depend on its Young's modulus, however. Plastic deformation mechanisms allow materials to be reshaped by external stresses well before the bonds between all subunits are broken. Indeed, it is this property that we are exploiting to efficiently drive shape change in a colloidal crystal. The onset of plastic deformation is a complex, material-dependent process; however, in metals it typically occurs at material strain conditions in the vicinity of 0.2% (42). For the example of 0.5-m colloids, this yielding strain would require a stress of $\approx 20\,\mathrm{nN/m}$, beyond which we should expect the mechanisms of plastic deformation to determine the strength of the assembly. Plastic deformation mechanisms in metals are predominantly dislocation-mediated processes, so by taking control of dislocations we may further control the mechanical properties of the assembly. For additional discussion, see the work of Gerbode et al. (43) for dislocation pinning in 2D colloidal materials and VanSaders and Glotzer (44) for pinning in 3D.

Dislocation Emitters in 3D Materials. The proposed dislocation-based reconfiguration scheme can be naturally extended to 3D

crystalline materials, albeit with additional considerations that warrant further study. Consider 2D emitters presented here as slices of a 3D material; the crystal could be extended indefinitely into the third dimension. This would transform the shown circular crystallites into crystalline fibers, with the embedded cluster a fiber-like core with cross-section as shown in *SI Appendix*, Fig. S4. To limit the fiber-like emitting cluster to a finite size, we can consider looping the fiber around and joining the ends. This cluster, now a fiber joined into a loop, would through swelling produce a dislocation line along its length. This would naturally produce a dislocation loop.

Such loops are stable, mobile defects in some crystalline systems (45). However, additional complications can arise in some cases. In 2D, a complementary pair of dislocations are produced through the action of the cluster, and in 3D a pair of loops would be created. These loops may not have the same mobilities or even stability in the crystalline system (46). For example, in many face-centered cubic materials the interstitial (or extrinsic) loop is stable and mobile, while the vacancy (or intrinsic) loop is unstable and decomposes into other defect species once created. Therefore, using loops to reconfigure 3D materials is possible, but further study is needed to understand the limitations of loop stability and mobility.

Dislocations as Metamodules. The dislocation-mediated material transport presented here can be compared to other schemes to redistribute mass within a (macroscopic) robotic swarm. When a reconfigurable robot is composed of densely packed incompressible subunits (modules), the motion of modules to enable ensemble reshaping must occur entirely on the surface, as there is no room for modules to move through the bulk. As the number of modules in a robot is increased, the surface area grows much slower than the volume. Therefore, for large numbers of modules this surface restriction is a potential limitation that could cap the reconfiguration rate (12). Designs like the Crystalline Robot (4) and the Telecube (5) aimed to address this issue by making modules capable of expansion or contraction. In these robots modules contract in sequence, transporting mass through the bulk of the robot array under detailed algorithmic control of all module docking/undocking steps. However, this mode of operation shares similarities to a family of crystalline defects that include dislocation loops and crowdions. In a crowdion, a linear chain of N crystal lattice sites have $N+1$ (interstitial type) or $N-1$ (vacancy type) particles occupying them (47). Similarly, dislocation loops are arrangements of crystal lattice planes where $N+1$ or $N-1$ planes occupy the space of N planes in a distributed manner. Unlike more common interstitials and vacancies, the extra or missing particle(s) is (are) not localized to a single site, but instead effectively spread out over many sites with fractional occupancy. Ensembles of cubes simulated with thermal agitation have been shown to display vacancy-type crowdions as an emergent behavior (48, 49). This suggests that stochastic versions of cube-type lattice robots might display crowdion-type mass transport without careful algorithmic control of neighbor bonding and only mild module compressibility. Dislocation loops are a more general phenomenon, for instance possible in face-centered cubic crystals (45).

Bulk reconfiguration has also been proposed in incompressible lattice robots. Clearly, insufficient room exists to efficiently transport modules through a space-filling or dense-packed bulk, so authors have proposed porous assembly types that alleviate this issue (12, 50–52). This shifts the focus of reconfiguration planning away from individual modules to groups of modules (referred to as metamodules), which maintain an open structure. The concept of a metamodule that maintains a sufficiently low density to permit transport can be directly compared to a dislocation. Dislocations are emergent phenomena that exactly perform the task that metamodules are designed for. Bulk material shape change results in "on-the-fly" dislocation creation to transport mass and enable plastic deformation. Rosa et al. (51) proposed a similar concept in the form of open holes that are shepherded around the interior of a lattice robot. These holes perform the dual function of transporting (negative) mass through the bulk and providing a low-density environment to allow for reconfiguration. From the behavior of crystalline materials under deforming stresses, we know that such holes are not the lowest free-energy motif that accomplishes these goals; instead, nature has selected dislocations as its metamodule of choice.

The ability of lattice robots to employ dislocations as on-demand emergent metamodules will depend upon the connection type present between neighbors. Many proposed crystalline robots have rigid connections between neighbors that are toggled according to algorithmic planning (4–6, 11). This process of latching onto a new neighbor represents a significant fraction of the difficulty of creating functional prototypes. Others have shown that near-isotropic bonding between neighbors is also a feasible strategy for robot design without a well-defined crystal structure (8, 9). However, we show here that isotropic subunit interactions coupled with a crystalline arrangement unlock the potential of using dislocations as emergent metamodules. Lattice robots with stiff, angle-dependent interactions are equivalent to covalently or ionically bonded materials. Dislocations are typically not important to the deformation of these materials, with fracture instead being the primary mode of shape change. For robotics applications, particularly during reconfiguration, the ensemble is desired to behave more like a ductile metal. The potential power of our work lies in the scalability of employing dislocations. Since dislocations are emergent, stable structures with high mobility, no control need be exerted to maintain them as they migrate. In our scheme, only the collective action of a small number of subunits together is sufficient to create and move dislocations, thereby reshaping the larger domain.

Conclusion

In this study we simulated a 2D colloidal system in which clusters of tunable-diameter particles are embedded. By cyclic swelling and shrinking of the particles in these clusters, dislocations were created and motivated to glide. Through design of the cluster shape, dislocation emission and migration can be strongly biased. Biased dislocation emitters fundamentally exert a shear slip effect, and by arranging multiple emitters in different configurations, different compound operations can be accomplished. This work presents an alternative mechanism for sculpting colloidal crystallites. We also explored how dislocations fulfill for colloids the role sought by metamodules in lattice robotics research and suggest that dislocations should be considered as a fundamental unit of reconfiguration in those systems as well.

Materials and Methods

All MD simulations reported here were performed with HOOMD-blue (v2.0) (53, 54). Simulations were run using the Extreme Science and Engineering Discovery Environment (XSEDE) (55). All particles interact through a shifted Lennard-Jones potential (56), where the origin is shifted so that the surface of the particle is the potential's zero isoenergy surface. The value of σ used in this potential was set to 0.75, and the radial shifting was chosen so that the minimum (located at $\sigma 2^{1/6}$ in the unshifted case) is at a distance of $D_0 = 2^{1/6}$. This distance is the minimum-energy isosurface of the pair potential and is taken to represent the particle's physical surface. The depth of the attractive well was set to $\epsilon = 1$. Simulations were carried out via Brownian integration as implemented in HOOMD-blue. System thermal energy was held at $kT/\epsilon = 0.22$, and particle mass was fixed at $m = 1$ (in simulation units). References in the text to energy, mass, time, and length scales will use these values for nondimensionalization. System temperature and pair potential parameters were chosen to produce solid-phase crystallites with realistic defect dynamics.

During a swelling or shrinking cycle, a cluster composed of a subset of particles changes its diameter by changing the radial shift applied to the

pair potential in small discrete increments (relative to the average distance between particles). The value of ϵ and σ used in the pair potential is kept constant at all times. These tunable-diameter particles are harmonically bonded to each other. The length of this harmonic bond is scaled along with the particle diameters during a simulation.

Renderings of particle simulations use a consistent color scheme, described in the Fig. 3 legend. To determine this coloring, the pair correlation function $g(r)$ is computed for the entire system, and the coordination number of a particle is determined by counting neighbors within a cutoff of $\frac{4}{3}D_0$ (approximately halfway between the first and second peaks in $g(r)$).

Data Availability. All study data are included in this article and *SI Appendix*.

ACKNOWLEDGMENTS. This work was supported as part of the Center for Bio-Inspired Energy Science, an Energy Frontier Research Center funded by the US Department of Energy, Office of Science, Basic Energy Sciences under Award DE-SC0000989. B.V.S. acknowledges a University of Michigan Rackham Predoctoral Fellowship. This research utilized computational resources and services supported by Advanced Research Computing at the University of Michigan, Ann Arbor, and used the Extreme Science and Engineering Discovery Environment (XSEDE), which is supported by NSF Grant ACI-1053575 (XSEDE Award DMR 140129).

1. E. Yablonovitch, T. J. Gmitter, K. M. Leung, Photonic band structure: The face-centered-cubic case employing nonspherical atoms. *Phys. Rev. Lett.* **67**, 2295–2298 (1991).
2. H. O. Moser, B. D. F. Casse, O. Wilhelmi, B. T. Saw, Terahertz response of a microfabricated rod–split-ring-resonator electromagnetic metamaterial. *Phys. Rev. Lett.* **94**, 063901 (2005).
3. A. Brunete *et al.*, Current trends in reconfigurable modular robots design. *Int. J. Adv. Rob. Syst.* **14**, 1729881417710457 (2017).
4. D. Rus, M. Vona, Crystalline robots: Self-reconfiguration with compressible unit modules. *Aut. Robots* **10**, 107–124 (2001).
5. J. W. Suh, S. B. Homans, M. Yim, "Telecubes: mechanical design of a module for self-reconfigurable robotics" in *Proceedings 2002 IEEE International Conference on Robotics and Automation* (IEEE, 2002), vol. 4, pp. 4095–4101.
6. K. Gilpin, A. Knaian, D. Rus, "Robot pebbles: One centimeter modules for programmable matter through self-disassembly" in *2010 IEEE International Conference on Robotics and Automation* (IEEE, 2010), pp. 2485–2492.
7. S. C. Goldstein, J. D. Campbell, T. C. Mowry, Programmable matter. *Computer* **38**, 99–101 (2005).
8. M. Shimizu, A. Ishiguro, T. Kawakatsu, "Slimebot: A Modular Robot That Exploits Emergent Phenomena" in *Proceedings of the 2005 IEEE International Conference on Robotics and Automation* (IEEE, 2005), pp. 2982–2987.
9. S. Li *et al.*, Particle robotics based on statistical mechanics of loosely coupled components. *Nature* **567**, 361–365 (2019).
10. R. Fitch, Z. Butler, Million module march: Scalable locomotion for large self-reconfiguring robots. *Int. J. Robot Res.* **27**, 331–343 (2008).
11. G. Aloupis *et al.*, Linear reconfiguration of cube-style modular robots. *Comput. Geom.* **42**, 652–663 (2009).
12. J. Lengiewicz, P. Hołobut, Efficient collective shape shifting and locomotion of massively-modular robotic structures. *Aut. Robots* **43**, 97–122 (2019).
13. M. Rubenstein, A. Cornejo, R. Nagpal, Programmable self-assembly in a thousand-robot swarm. *Science* **345**, 795–799 (2014).
14. J. Palacci, S. Sacanna, A. P. Steinberg, D. J. Pine, P. M. Chaikin, Living crystals of light-activated colloidal surfers. *Science* **339**, 936–940 (2013).
15. A. Altemose *et al.*, Chemically controlled spatiotemporal oscillations of colloidal assemblies. *Angew. Chem. Int. Ed.* **56**, 7817–7821 (2017).
16. J. Yu, B. Wang, X. Du, Q. Wang, L. Zhang, Ultra-extensible ribbon-like magnetic microswarm. *Nat. Commun.* **9**, 3260 (2018).
17. B. Wang *et al.*, Reconfigurable swarms of ferromagnetic colloids for enhanced local hyperthermia. *Adv. Funct. Mater.* **28**, 1705701 (2018).
18. B. Yigit, Y. Alapan, M. Sitti, Programmable collective behavior in dynamically self-assembled mobile microrobotic swarms. *Adv. Sci.* **6**, 1801837 (2019).
19. H. Massana-Cid, F. Meng, D. Matsunaga, R. Golestanian, P. Tierno, Tunable self-healing of magnetically propelling colloidal carpets. *Nat. Commun.* **10**, 2444 (2019).
20. H. Xie *et al.*, Reconfigurable magnetic microrobot swarm: Multimode transformation, locomotion, and manipulation. *Sci. Robot.* **4**, eaav8006 (2019).
21. W. T. M. Irvine, A. D. Hollingsworth, D. G. Grier, P. M. Chaikin, Dislocation reactions, grain boundaries, and irreversibility in two-dimensional lattices using topological tweezers. *Proc. Natl. Acad. Sci. U.S.A.* **110**, 15544–15548 (2013).
22. P. Schall, I. Cohen, D. A. Weitz, F. Spaepen, Visualizing dislocation nucleation by indenting colloidal crystals. *Nature* **440**, 319–323 (2006).
23. W. T. M. Irvine, V. Vitelli, P. M. Chaikin, Pleats in crystals on curved surfaces. *Nature* **468**, 947 (2010).
24. F. A. Lavergne, A. Curran, D. G. A. L. Aarts, R. P. A. Dullens, Dislocation-controlled formation and kinetics of grain boundary loops in two-dimensional crystals. *Proc. Natl. Acad. Sci. U.S.A.* **115**, 6922–6927 (2018).
25. G. E. Fernandes, D. J. Beltran-Villegas, M. A. Bevan, Interfacial colloidal crystallization via tunable hydrogel depletants. *Langmuir* **24**, 10776–10785 (2008).
26. T. Gong, D. T. Wu, D. W. M. Marr, Two-dimensional electrohydrodynamically induced colloidal phases. *Langmuir* **18**, 10064–10067 (2002).
27. S. O. Lumsdon, E. W. Kaler, O. D. Velev, Two-dimensional crystallization of microspheres by a coplanar AC electric field. *Langmuir* **20**, 2108–2116 (2004).
28. D. Du, D. Li, M. Thakur, S. L. Biswal, Generating an in situ tunable interaction potential for probing 2-D colloidal phase behavior. *Soft Matter* **9**, 6867–6875 (2013).
29. P. L. Biancaniello, A. J. Kim, J. C. Crocker, Colloidal interactions and self-assembly using DNA hybridization. *Phys. Rev. Lett.* **94**, 058302 (2005).
30. M. Grzelczak, J. Vermant, E. M. Furst, L. M. Liz-Marzán, Directed self-assembly of nanoparticles. *ACS Nano* **4**, 3591–3605 (2010).
31. V. Lotito, T. Zambelli, Approaches to self-assembly of colloidal monolayers: A guide for nanotechnologists. *Adv. Colloid Interface Sci.* **246**, 217–274 (2017).
32. H. Senff, W. Richtering, Temperature sensitive microgel suspensions: Colloidal phase behavior and rheology of soft spheres. *J. Chem. Phys.* **111**, 1705–1711 (1999).
33. J. Zhang, X. Jiang, Y. Zhang, Y. Li, S. Liu, Facile fabrication of reversible core cross-linked micelles possessing thermosensitive swellability. *Macromolecules* **40**, 9125–9132 (2007).
34. X. Jiang, Z. Ge, J. Xu, H. Liu, S. Liu, Fabrication of multiresponsive shell cross-linked micelles possessing pH-controllable core swellability and thermo-tunable corona permeability. *Biomacromolecules* **8**, 3184–3192 (2007).
35. J. A. Mason *et al.*, Contraction and expansion of stimuli-responsive DNA bonds in flexible colloidal crystals. *J. Am. Chem. Soc.* **138**, 8722–8725 (2016).
36. I. Gorelikov, L. M. Field, E. Kumacheva, Hybrid microgels photoresponsive in the near-infrared spectral range. *J. Am. Chem. Soc.* **126**, 15938–15939 (2004).
37. B. VanSaders, J. Dshemuchadse, S. C. Glotzer, Strain fields in repulsive colloidal crystals. *Phys. Rev. Mater.* **2**, 063604 (2018).
38. A. Einstein, *Investigations on the Theory of the Brownian Movement* (Dover Publications, New York, NY, 1956).
39. T. R. Matzelle, G. Geuskens, N. Kruse, Elastic properties of poly(N-isopropylacrylamide) and poly(acrylamide) hydrogels studied by scanning force microscopy. *Macromolecules* **36**, 2926–2931 (2003).
40. D. G. Grier, Y. Roichman, Holographic optical trapping. *Appl. Optic.* **45**, 880–887 (2006).
41. Y. Yin, Y. Lu, B. Gates, Y. Xia, Template-assisted self-assembly: A practical route to complex aggregates of monodispersed colloids with well-defined sizes, shapes, and structures. *J. Am. Chem. Soc.* **123**, 8718–8729 (2001).
42. W. Callister, D. Rethwisch, *Fundamentals of Material Science and Engineering: An Integrated Approach* (John Wiley & Sons, Hoboken, NJ, 2008).
43. S. J. Gerbode, S. H. Lee, C. M. Liddell, I. Cohen, Restricted dislocation motion in crystals of colloidal dimer particles. *Phys. Rev. Lett.* **101**, 058302 (2008).
44. B. VanSaders, S. C. Glotzer, Pinning dislocations in colloidal crystals with active particles that seek stacking faults. *Soft Matter* **16**, 4182–4291 (2020).
45. B. VanSaders, S. C. Glotzer, Designing active particles for colloidal microstructure manipulation via strain field alchemy. *Soft Matter* **15**, 6086–6096 (2019).
46. Y. N. Osetsky, D. J. Bacon, A. Serra, B. N. Singh, S. I. Golubov, Stability and mobility of defect clusters and dislocation loops in metals. *J. Nucl. Mater.* **276**, 65–77 (2000).
47. H. R. Paneth, The mechanism of self-diffusion in alkali metals. *Phys. Rev.* **80**, 708–711 (1950).
48. F. Smallenburg, L. Filion, M. Marechal, M. Dijkstra, Vacancy-stabilized crystalline order in hard cubes. *Proc. Natl. Acad. Sci. U.S.A.* **109**, 17886–17890 (2012).
49. B. van der Meer, R. van Damme, M. Dijkstra, F. Smallenburg, L. Filion, Revealing a vacancy analog of the crowdion interstitial in simple cubic crystals. *Phys. Rev. Lett.* **121**, 258001 (2018).
50. K. Stoy, R. Nagpal, "Self-repair through scale independent self-reconfiguration" in *2004 IEEE/RSJ International Conference on Intelligent Robots and Systems (IROS)* (IEEE, 2004), vol. 2, pp. 2062–2067.
51. M. De Rosa, S. Goldstein, P. Lee, J. Campbell, P. Pillai, "Scalable shape sculpting via hole motion: motion planning in lattice-constrained modular robots" in *Proceedings 2006 IEEE International Conference on Robotics and Automation* (IEEE, 2006), pp. 1462–1468.
52. D. J. Dewey *et al.*, "Generalizing metamodules to simplify planning in modular robotic systems" in *2008 IEEE/RSJ International Conference on Intelligent Robots and Systems* (IEEE, 2008), pp. 1338–1345.
53. J. A. Anderson, C. D. Lorenz, A. Travesset, General purpose molecular dynamics simulations fully implemented on graphics processing units. *J. Comput. Phys.* **227**, 5342–5359 (2008).
54. J. Glaser *et al.*, Strong scaling of general-purpose molecular dynamics simulations on GPUs. *Comput. Phys. Commun.* **192**, 97–107 (2015).
55. J. Towns *et al.*, Xsede: Accelerating scientific discovery. *Comput. Sci. Eng.* **16**, 62–74 (2014).
56. J. E. Jones, D. Sc, On the determination of molecular fields. –II. From the equation of state of a gas. *Proc. R. Soc. Lond. A* **106**, 463–477 (1924).